

## NEW HUBBLE SPACE TELESCOPE WFC3/UVIS OBSERVATIONS AUGMENT THE STELLAR-POPULATION COMPLEXITY OF $\omega$ CENTAURI\*

A. BELLINI<sup>1,2,5</sup>, L. R. BEDIN<sup>2</sup>, G. PIOTTO<sup>1</sup>, A. P. MILONE<sup>1</sup>, A. F. MARINO<sup>1,3</sup>, AND S. VILLANOVA<sup>4</sup>

<sup>1</sup> Dipartimento di Astronomia, Università di Padova, vicolo dell’Osservatorio 3, 35122 Padova, Italy; bellini@stsci.edu

<sup>2</sup> Space Telescope Science Institute, 3700 San Martin Drive, Baltimore, MD 21218, USA

<sup>3</sup> Departamento de Astronomía y Astrofísica, Pontificia Universidad Católica de Chile, Casilla 306, Santiago 22, Chile

<sup>4</sup> Departamento de Astronomía, Universidad de Concepción, Casilla 160-C, Concepción, Chile

Received 2010 February 22; accepted 2010 June 19; published 2010 July 15

### ABSTRACT

We used archival multi-band *Hubble Space Telescope* observations obtained with the Wide Field Camera 3 in the UV-optical channel to present important new observational findings on the color-magnitude diagram (CMD) of the Galactic globular cluster  $\omega$  Centauri. The UV WFC3 data have been coupled with available Wide Field Channel/Advanced Camera for Surveys optical-band data. The new CMDs, obtained from the combination of colors coming from eight different bands, disclose an even more complex stellar population than previously identified. This paper discusses the detailed morphology of the CMDs.

**Key words:** catalogs – globular clusters: individual (NGC 5139) – Hertzsprung–Russell and C–M diagrams – stars: Population II

**Online-only material:** color figures

### 1. INTRODUCTION

$\omega$  Centauri is the most studied and the most enigmatic among the Milky Way satellites. For a long time it has been considered a globular cluster, but a number of peculiarities, such as its mass, its chemical composition, its stellar content, and its kinematics, suggest that it might be the remnant of a larger stellar system (Bekki & Freeman 2003; Lee et al. 2009, and references therein).

Since the discovery that its stars span a wide range of metallicities, including iron-peak elements (Cannon & Stobie 1973; Freeman & Rodgers 1975; Johnson et al. 2009, and references therein), great interest and great efforts have been dedicated to it.

With the advent of wide-field imagers, and thanks to the increasingly high photometric precision in the densest cluster regions, new discoveries have revived interest in  $\omega$  Cen, and complicated the already inexplicable enigma represented by its composite stellar population. Lee et al. (1999) and Pancino et al. (2000) announced that its red giant branch (RGB) resolves into several distinct stellar sequences. Anderson (1997) found that over a range of about 2 mag, the main sequence (MS) splits into a blue (bMS) and a red sequence (rMS). This result has been confirmed by Bedin et al. (2004), who discovered a third, less populated MS (MS-a) on the red side of the rMS (see also Villanova et al. 2007, hereafter V07). A totally unexpected discovery came from the spectroscopic analysis by Piotto et al. (2005), who revealed that the bMS is more metal-rich than the rMS. Only greatly enhanced helium can explain the color and metallicity difference between the two MSs. Bellini et al. (2009; see also Sollima et al. 2007) found that bMS stars are more centrally concentrated than rMS ones, with a bMS over rMS ratio ranging from  $\sim 1.0$  ( $r \lesssim 2.5'$ ) to  $\sim 0.40$  ( $r \gtrsim 8'$ ).

Perhaps the most complex region of the color-magnitude diagram (CMD) is the sub-giant branch (SGB). Photometric

studies showed that the SGB of  $\omega$  Cen is split into four or possibly five distinct stellar populations (Lee et al. 2005; Sollima et al. 2005; Villanova et al. 2007).

In this work, we present high-accuracy photometry obtained with both the Wide Field Camera 3 (WFC3) in the UV-optical channel (UVIS), and the Wide Field Channel of the Advanced Camera for Surveys (WFC/ACS) of the *Hubble Space Telescope* (*HST*). Not surprisingly, we obtained astonishingly complex CMDs unveiling a number of new details which make the  $\omega$  Cen stellar population appear even more complex than previously shown, and create a real challenge for understanding the star formation history in this cluster.

The purpose of this work is to present these new CMDs to the astronomical community, discuss their detailed morphology—with the hope of adding important information and deeper insight into  $\omega$  Cen—and help to add up all the pieces of what still remains a broken puzzle. The multi-band astro-photometric catalog presented in this work will be publicly available to the astronomical community for further analysis.

### 2. OBSERVATIONS, MEASUREMENTS, AND SELECTIONS

For calibration purposes,  $\omega$  Cen has been observed many times with *HST*, using a wide variety of filters. Recent observations were collected with the newly installed WFC3. On 2009 September 9, a set of well-dithered exposures through the broadband UV filters F225W, F275W, and F336W were released to the community. The data were collected on 2009 July 15 for general calibration purposes (PID-11452). The portion of the data that we used in this paper consists of nine exposures, each of 350 s, for each filter. The archive images were standard pipeline pre-reduced FLT, and we measured star positions and fluxes with software mostly based on img2xym\_WFI (Anderson et al. 2006). Details of this software will be presented in a stand-alone paper. Star positions and fluxes have been corrected for geometric distortion and pixel area using the geometric distortion solution provided by Bellini & Bedin (2009), and calibrated as in Bedin et al. (2005).

\* Based on observations with the NASA/ESA *Hubble Space Telescope*, obtained at the Space Telescope Science Institute, which is operated by AURA, Inc., under NASA contract NAS 5-26555.

<sup>5</sup> Visiting PhD Student at STScI under the “2008 Graduate Research Assistantship” program.

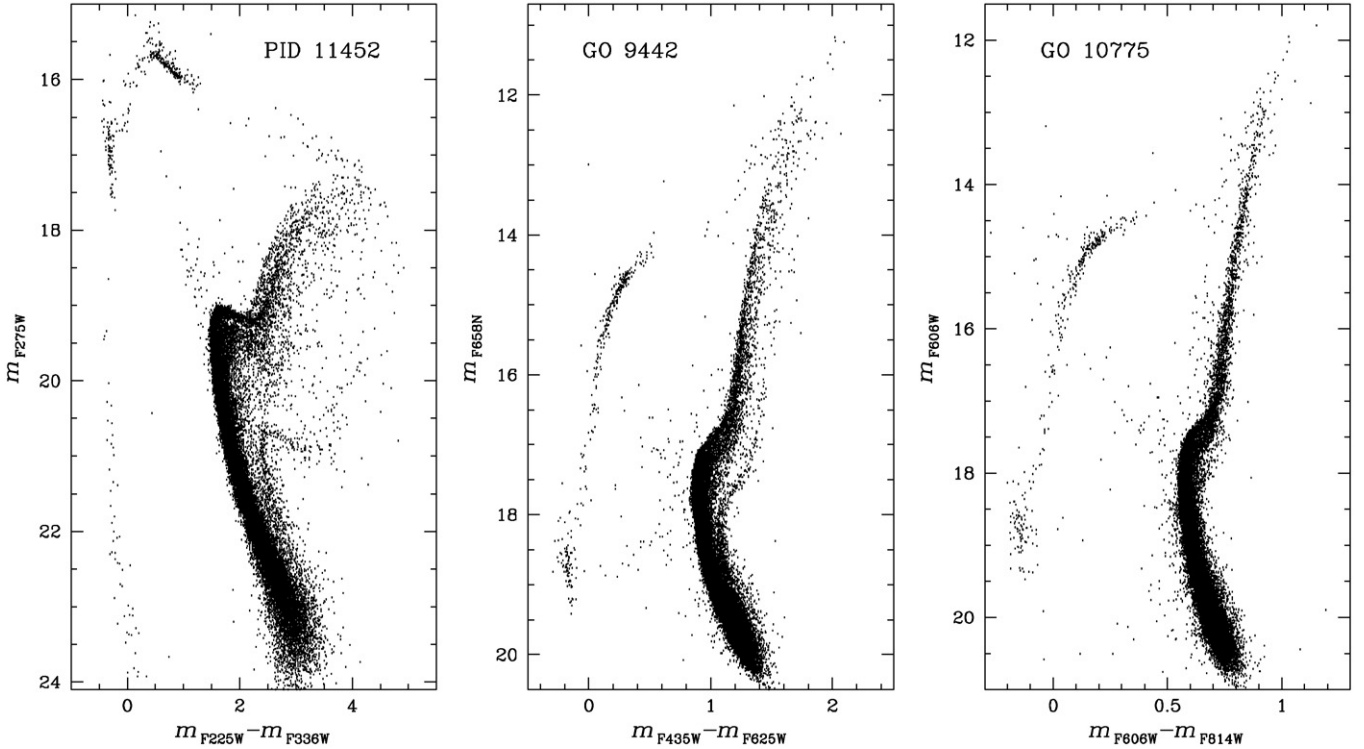


**Figure 1.** Collection of CMDs from our three data sets: the WFC3/UVIS CMD in the UV filters  $m_{F275W}$  vs.  $m_{F225W} - m_{F336W}$ , from PID-11452 (left); the ACS/WFC  $m_{F658N}$  vs.  $m_{F435W} - m_{F625W}$  CMD, from GO-9442 (center); and the ACS/WFC  $m_{F606W}$  vs.  $m_{F606W} - m_{F814W}$  CMD, from GO-10775 (right). We plotted only the best  $\sim 32,000$  stars in common among the three data sets (see the text for details).

We complement these UV data with the optical photometry obtained with the ACS/WFC in the filters F435W, F625W, F658N, F606W, and F814W. Details on these data sets and their photometry can be found in V07 and Anderson et al. (2008).

Since we are focused on high-accuracy photometry, this work only concerns relatively isolated stars with small photometric and astrometric errors, and high point-spread function (PSF)-fit quality. A detailed description of the selection procedures adopted in this paper is given in Milone et al. (2009). Finally, we corrected our photometry for both reddening variations in the field of view (FoV) and spatial-dependent photometric errors, introduced by small variations of the PSF shape, which are not accounted for in our PSF models. To achieve this aim, we used a method similar to that used by Sarajedini et al. (2007) and Milone et al. (2008). Briefly, we determined the average MS ridge line (RL) for each CMD, and then analyzed the color residuals as a function of the position within the FoV. We corrected the effect of spatial photometric variations suffered by each star by computing the average color residuals from the MS RL of its 50 well-measured neighbors and then correcting the star color by this amount.

### 3. COLOR–MAGNITUDE DIAGRAMS

Figure 1 shows a collection of CMDs from multi-band WFC3/UVIS and ACS/WFC photometry. All CMDs encompass all the evolutionary sequences, from faint MS stars down to a well-developed white dwarf cooling sequence (see Figure 1). A close examination of these CMDs leads to the realization that each of them is a mine of information on the stellar content of  $\omega$  Cen. A model-based interpretation of these CMDs is severely complicated by the heterogeneity of the composition of each sequence and by possible age differences, and requires

a very accurate analysis, which is beyond the purpose of this paper.

Many of the features that we observe in these CMDs are well known and widely studied. For completeness of information, and in order to make the following discussion clearer to the reader, in Figure 2 (left panel) we show the CMD resulting from the  $10 \times 10$  arcmin $^2$  mosaic of ACS images centered on the cluster center that was already analyzed in several papers (Bedin et al. 2004; V07; Cassisi et al. 2009; Bellini et al. 2009; D’Antona et al. 2010). The high accuracy of the ACS photometry had already revealed a large number of evolutionary sequences in the CMD. We used Hess diagrams on the right panels of Figure 2 to highlight the four main SGBs and the triple MS, following the notation of V07.

In the following, we will focus our attention on a number of details in the CMD that are revealed for the first time by the high-accuracy multi-band photometry presented in this paper.

#### 3.1. The Triple Main Sequence

The new, multi-band data set provided by WFC3, combined with the ACS data, opens a new observational window on the complex MS of  $\omega$  Cen.

The wide color baseline of the  $m_{F814W}$  versus  $m_{F275W} - m_{F814W}$  CMD plotted in the left panel of Figure 3 allows us to isolate the two groups of bMS and rMS stars indicated by blue and red color-coded regions. Similarly, we can select a sample of MS-a stars from the  $m_{F435W}$  versus  $m_{F336W} - m_{F435W}$  CMD where the MS-a is most clearly separated from the remaining MSs of  $\omega$  Cen. Selected stars are highlighted in green in the right panel CMD of Figure 3.

We have high-accuracy photometric measurements in eight bands, which allow us to plot seven distinct CMDs involving the F814W band. For each of them, we plotted  $m_{F814W}$  magnitudes

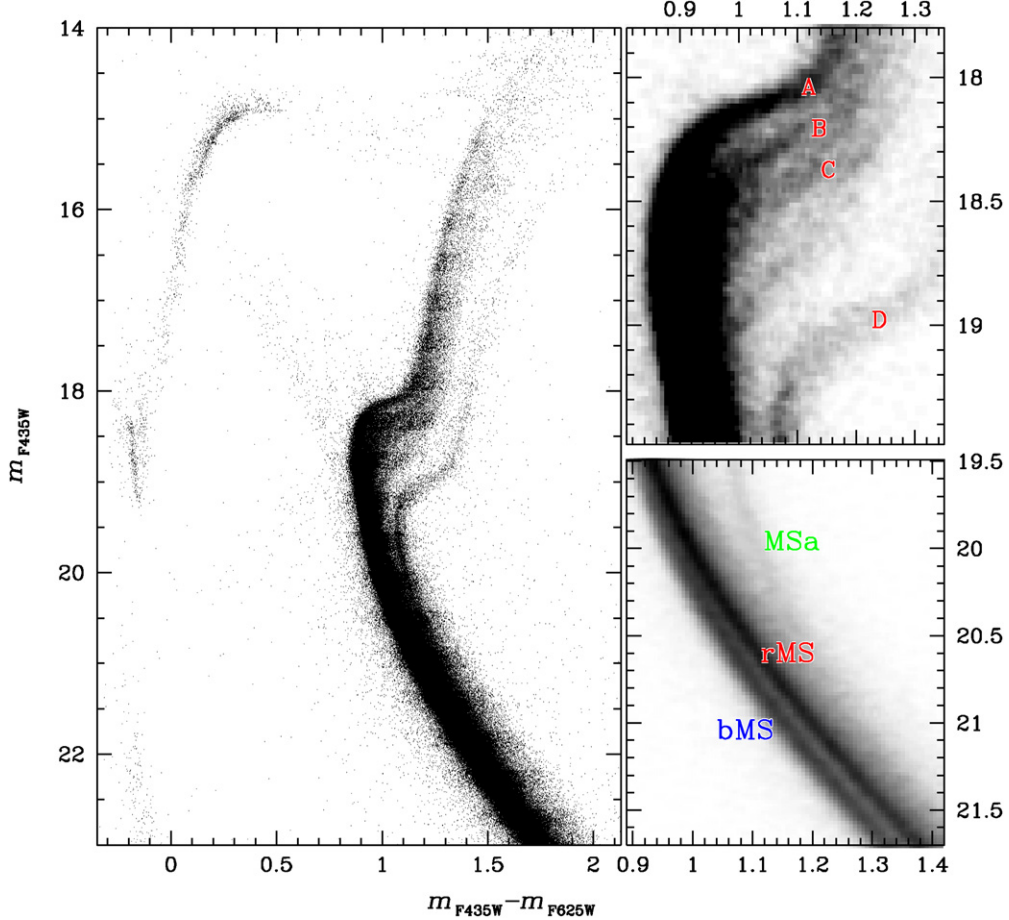


**Figure 2.** Definition of the main CMD branches used in this paper.

(A color version of this figure is available in the online journal.)

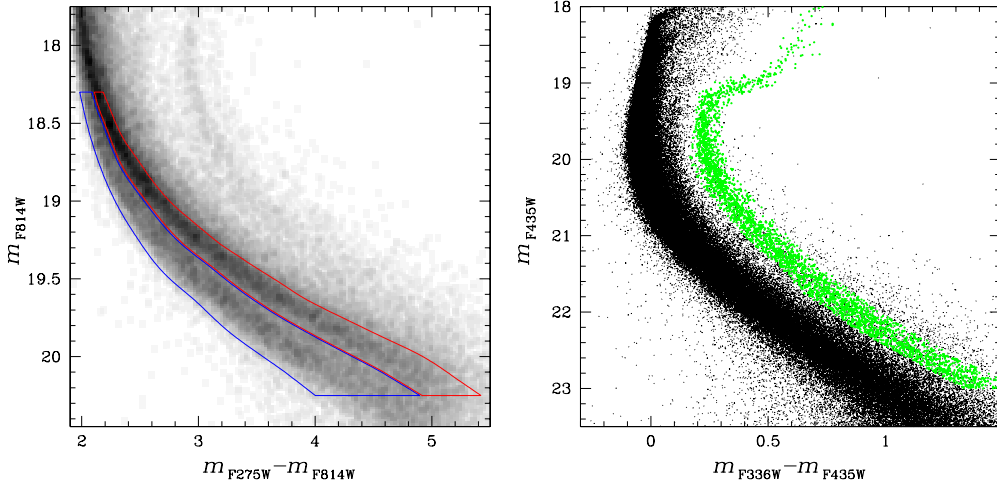


**Figure 3.** Left: selection of bMS (blue boundary) and rMS (red boundary) stars. Right: selection of MS-a (green points) stars.

(A color version of this figure is available in the online journal.)

as a function of the  $m_X - m_{F814W}$  color, where  $m_X = m_{F225W}$ ,  $m_{F275W}$ ,  $m_{F336W}$ ,  $m_{F435W}$ ,  $m_{F606W}$ ,  $m_{F625W}$  and  $m_{F658N}$ .

The bottom panels of Figure 4 show the three most representative of these CMDs (zoomed around the MS region). We assigned a blue, red, or green color code to each star according to whether it belongs to the bMS, rMS, or MS-a sample, as defined in Figure 3. In the upper panels of Figure 4, we superimposed the MS RLs corresponding to the three MSs, extracted from the

CMD using the method described in Milone et al. (2008) on the observed CMDs. Briefly, we divided the CMD into intervals of 0.2 mag in the F814W band and calculated the median color and magnitude for the bMS, rMS, and MS-a stars for each interval. We fitted these median points with a spline and obtained a first guess for the MS RL. Then, we calculated the difference between the color of each star and the color of the MS RL corresponding to the magnitude of the star, and we took as  $\sigma$  the

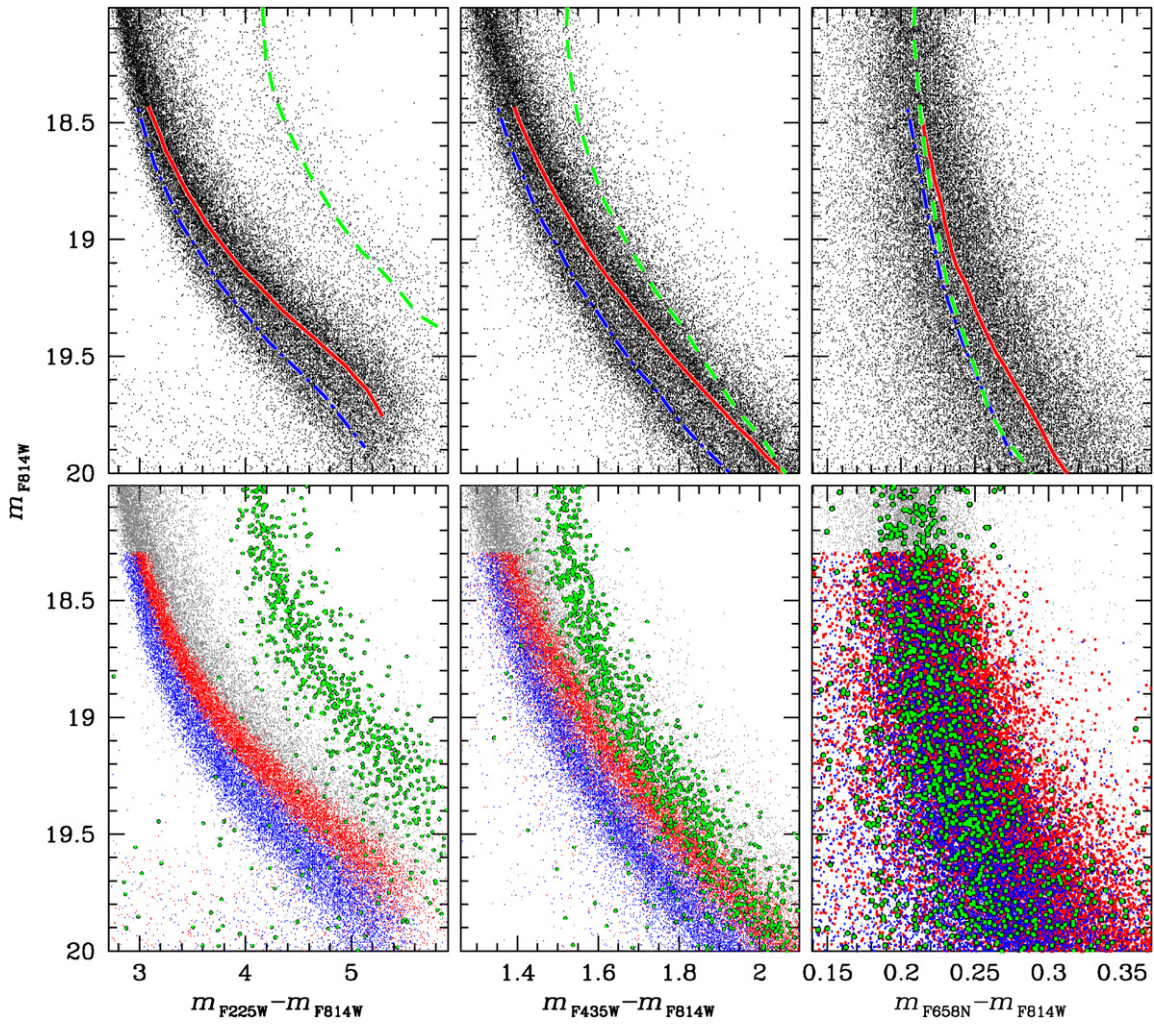


**Figure 4.** Example of the definition of the MS RLs.  
(A color version of this figure is available in the online journal.)

68.27th percentile of the absolute value of the color difference. We rejected all stars with color differences larger than  $4\sigma$  and we recalculated the median points.

The RLs for the three MSs are shown in Figure 5 for the seven CMDs analyzed in this section. We note some interesting features: (1) the RLs of the bMS and the MS-a are nearly parallel in all the CMDs in the magnitude range  $m_{F814W} \sim 18.5-20.0$ , while the RLs of the rMS have a different slope and (2) when using  $m_{F606W} - m_{F814W}$  and  $m_{F625W} - m_{F814W}$  colors the RL of the MS-a seems to intercept (or merge with) the rMS going from the brightest to the faintest stars. MS-a stars become even bluer than the rMS ones in the  $m_{F658N} - m_{F814W}$  color.

This is the most intriguing CMD, in terms of He content: He abundance affects the color of MS stars. The F658N filter essentially maps the H $\alpha$  feature with a very small influence by other elements. It measures the strength of the H $\alpha$  which, for MS stars cooler than 8000 K, is a function of  $T_{\text{eff}}$ , but also of the hydrogen content, if it is allowed to vary. MS-a stars are more metal-rich than rMS stars, being the progenitors of SGB-D and of the RGB-a (Pancino et al. 2002; V07). For this reason, the fact that MS-a stars become even bluer than the rMS in the  $m_{F658N} - m_{F814W}$  color, overlapping with the bMS, might imply that MS-a is also enriched in He (as suggested by Norris 2004). In fact, He enhancement tends to move the MS to bluer colors. The shape of the MS-a, parallel to the bMS, might also

be an indication that its stars are He enriched. However, we also know that the MS-a has higher iron content than the bMS. Higher metallicity implies redder MS colors. A combination of different metal abundances, including CNO, and He content results in the observed behavior of the MS-a color.

In order to quantify the color differences among the three MSs as a function of the color baseline, in Figure 6 we plotted the central wavelength  $\lambda$  of the  $m_X$  filter versus the measured color difference  $\Delta(\text{color})$  of both bMS stars (blue points) and MS-a stars (green points), with respect to the rMS RL color, at  $m_{F814W} = 19.4$  (this magnitude level is also indicated with a horizontal line in Figure 5).

The color distances plotted in Figure 6 are listed in Table 1.

### 3.2. The Intrinsic Broadening of the rMS

A visual inspection of the  $m_{F275W}$  versus  $m_{F275W} - m_{F336W}$  CMD of Figure 7 suggests that the rMS is broadened. In this section, we will investigate the possible presence of this intrinsic color spread among rMS stars, by using the same approach followed in recent studies on the MS broadening of 47 Tuc (Anderson et al. 2009) and of NGC 6752 (Milone et al. 2010).

We started by dividing F275W and F336W images in two halves (hereafter, samples 1 and 2), and considered only those stars measured in both sub-samples. From each of the two in-

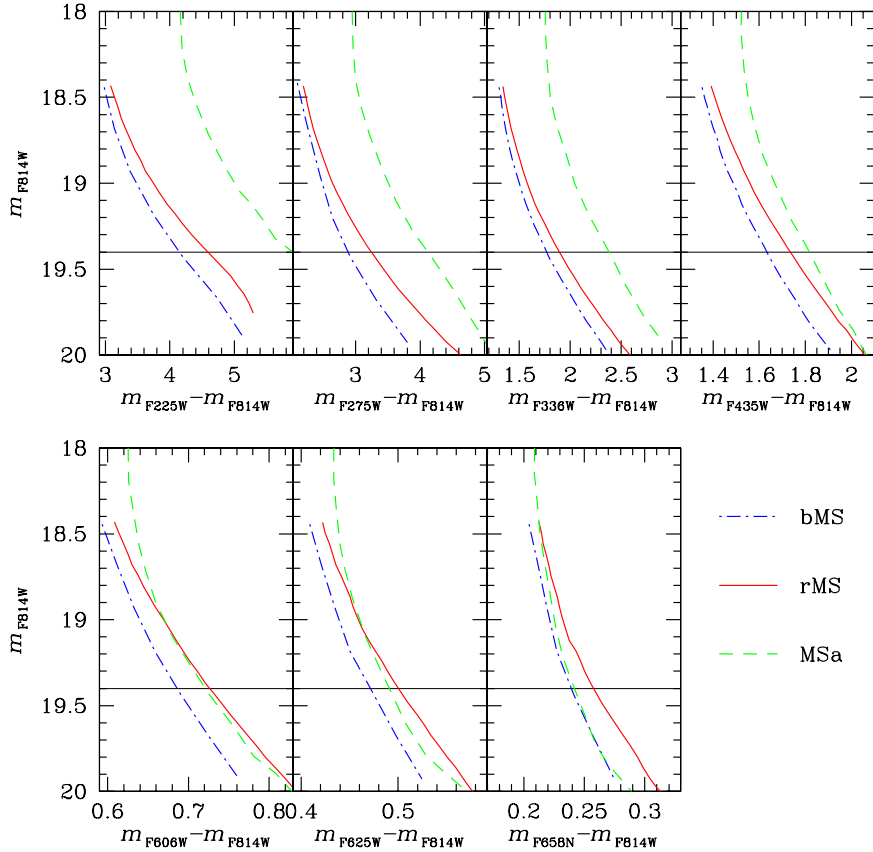


**Figure 5.** bMS and the MS-a run almost parallel in all CMDs. In some CMDs, the MS-a seems to cross the rMS.  
(A color version of this figure is available in the online journal.)

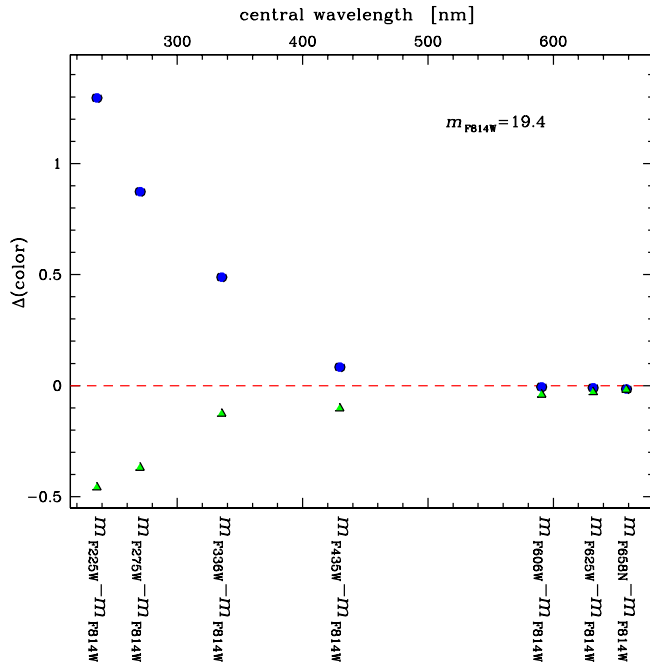


**Figure 6.** Color distance from the rMS RL for bMS stars (blue points) and MS-a stars (green triangles) at  $m_{F814W} = 19.4$ , plotted as a function of the central wavelength of the  $m_X$  filter.  
(A color version of this figure is available in the online journal.)

dependent subsets, we plotted a CMD. As an example we show the CMD from the first data set in panel (a) of Figure 8. The selected bMS and MS-a stars are represented with blue and green

**Table 1**  
Color Distances from the rMS RL for bMS Stars ( $\Delta_{\text{COLOR}}^{\text{bMS}}$ ) and MS-a Stars ( $\Delta_{\text{COLOR}}^{\text{MS-a}}$ ) at  $m_{F814W} = 19.4$

COLOR	$\Delta_{\text{COLOR}}^{\text{bMS}}$	$\Delta_{\text{COLOR}}^{\text{MS-a}}$
$m_{F225W} - m_{F814W}$	$1.30 \pm 0.01$	$-0.46 \pm 0.10$
$m_{F275W} - m_{F814W}$	$0.87 \pm 0.01$	$-0.37 \pm 0.10$
$m_{F336W} - m_{F814W}$	$0.49 \pm 0.01$	$-0.13 \pm 0.10$
$m_{F435W} - m_{F814W}$	$0.08 \pm 0.01$	$-0.10 \pm 0.10$
$m_{F606W} - m_{F814W}$	$-0.01 \pm 0.01$	$-0.04 \pm 0.10$
$m_{F625W} - m_{F814W}$	$-0.01 \pm 0.01$	$-0.03 \pm 0.10$
$m_{F658N} - m_{F814W}$	$-0.02 \pm 0.01$	$-0.02 \pm 0.10$

colors, while the rMS stars are plotted in red (in all the plots, star colors are given according to their classification, as defined in Figure 5). The dashed line is the RL of the rMS, obtained as described in the previous section. Then we subtracted the RL color at the same magnitude from the observed color (hereafter  $C$ ) of each star, obtaining the quantity  $\Delta C$ . The straightened MSs for the first and second data sets are plotted in panels (b) and (c), respectively. In panel (d), we show the color distribution of the straightened MS from the whole data set (indicated as  $(\Delta C_1 + \Delta C_2)/2$ ). In this case, the errors are smaller by a factor of  $\sqrt{2}$  with respect to those of the two data halves.

Panel (e) shows the distribution of the difference between the colors in each half of the images (i.e.,  $(\Delta C_1 - \Delta C_2)/2$ ) which is indicative of the color error. The histogram distributions of  $(\Delta C_1 + \Delta C_2)/2$  and  $(\Delta C_1 - \Delta C_2)/2$  are plotted in panels (f) and (g), respectively. In Table 2, we give the estimated values of the intrinsic and error dispersion of the rMS for four equally spaced magnitude intervals, assuming a Gaussian distribution.

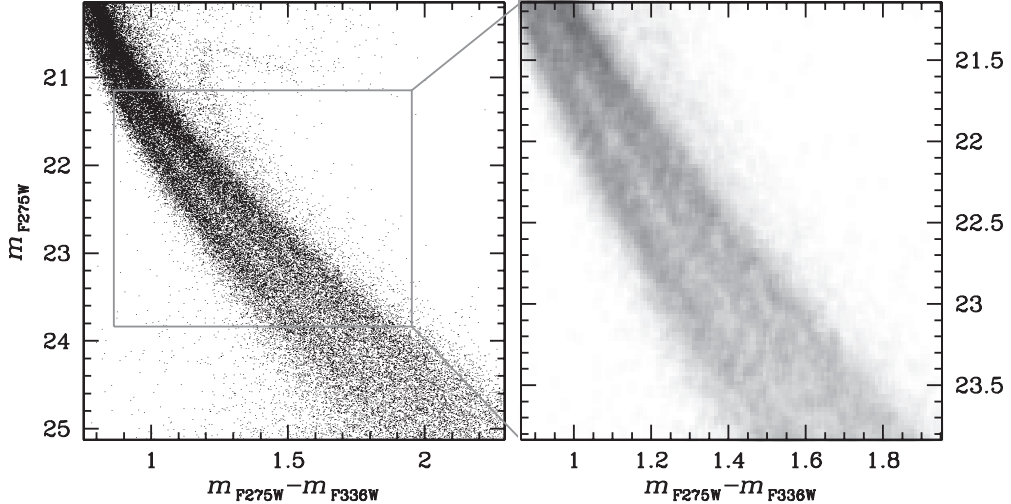


**Figure 7.** rMS is broadened (see the text for details).

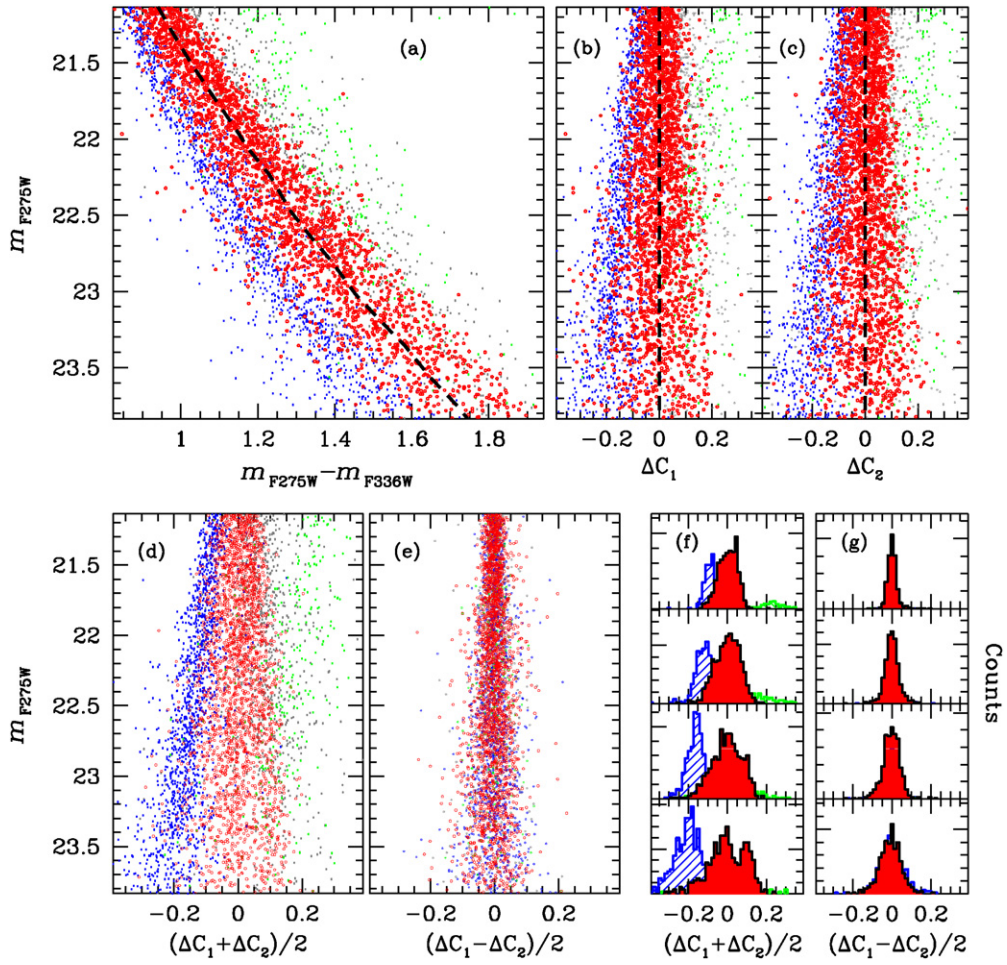


**Figure 8.** Evidence of the intrinsic broadening of the rMS (see the text for details).

(A color version of this figure is available in the online journal.)

As suggested by a visual inspection of panel (d), there is no doubt that the rMS is larger than that expected from the color–error distribution shown in panel (e).<sup>6</sup> Even in the worst case of the

last magnitude bin considered, we have an intrinsic dispersion of  $0.100 \pm 0.004$ , which is significantly larger (at the level of more than  $10\sigma$ ) than the error dispersion ( $0.051 \pm 0.002$ ).

Figure 7 and the bottom two panels of Column (f) of Figure 9 might suggest a possible split. We cannot assess the significance of this feature, but we think it is worthy of further investigation. As shown by V07, the rMS evolves into the brightest SGB-A sequence. The fact that the rMS is broadened will not come as a

<sup>6</sup> Note that we are aware of the significantly different efficiencies of the two CCDs of WFC3/UVIS toward UV. For this reason, thanks to the large dither pattern of the observations, we were able to repeat the analysis creating two subsamples made up with only one or the other CCD. We find (in the smaller region of the overlap) the same color distribution for the rMS.

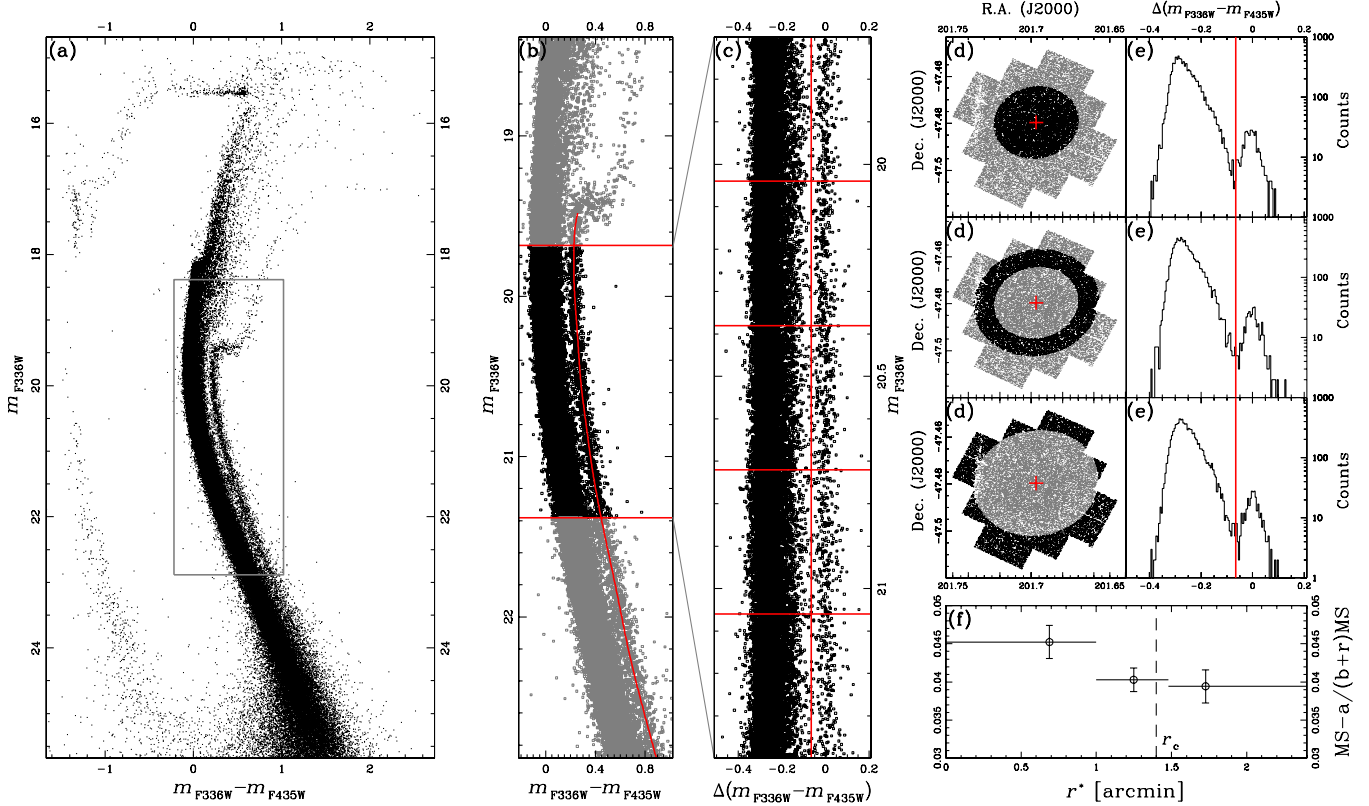


**Figure 9.** Panel (a) shows the  $m_{\text{F}336\text{W}}$  vs.  $m_{\text{F}336\text{W}} - m_{\text{F}435\text{W}}$  CMD. The region highlighted with the gray rectangle is zoomed-in in panel (b). The red fit marks the MS-a fiducial line. In panel (c), we show the rectified MSs in the magnitude interval  $19.7 < m_{\text{F}336\text{W}} < 21.4$ . The vertical red line separates MS-a members (on the right) from the rest of the MS stars (on the left). We defined three radial bins (panel (d)), each one containing the same number of selected stars. For each radial bin, we derived a color-distribution histogram (panel (e)). The radial distribution of the MS-a/(b+r)MS star-count ratio is shown in panel (f). The dashed line marks the core radius (Harris 1996).

(A color version of this figure is available in the online journal.)

**Table 2**

The Two Quantities Representing Estimates of Intrinsic Dispersion (Second Column), and Measurement Uncertainties (Third Column), in Four Different Magnitude Intervals (Indicated in the First Column)

$m_{\text{F}275\text{W}}$	$\sigma_{(\Delta C_1 + \Delta C_2)/2}$	$\sigma_{(\Delta C_1 - \Delta C_2)/2}$
21.13–21.81	$0.048 \pm 0.002$	$0.021 \pm 0.001$
21.81–22.48	$0.067 \pm 0.002$	$0.033 \pm 0.001$
22.48–23.16	$0.082 \pm 0.003$	$0.040 \pm 0.002$
23.16–23.83	$0.100 \pm 0.004$	$0.051 \pm 0.002$

surprise. In Piotto et al. (2005), stars in this sequence were found to have a large spread in C, much larger than that of stars on the bMS. If light-element abundances are correlated, as happens in all the massive clusters, this also implies a spread in N and O. We do not know the magnitude of this spread, but it surely must be reflected in the photometry, especially in the blue–UV filters where CH and CN bands are located.

### 3.3. The MS-a

The accurate CMDs presented in the previous sections also impose a more detailed investigation for the MS-a.

Among all color combinations, the  $m_{\text{F}336\text{W}} - m_{\text{F}435\text{W}}$  color is the one that provides us with the best separation between MS-a stars and the other MSs of  $\omega$  Cen. The reason could be that the MS-a has a somewhat peculiar CNO content with respect to the other populations. As outlined above, filters centered in the

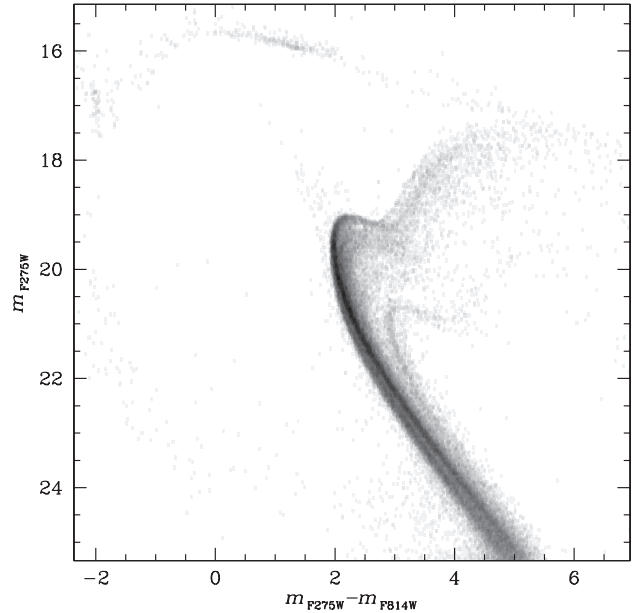


**Figure 10.** Hess diagram of the  $m_{\text{F}275\text{W}}$  vs.  $m_{\text{F}275\text{W}} - m_{\text{F}814\text{W}}$  CMD showing the complexity of  $\omega$  Cen.

blue–ultraviolet region, between  $\sim 3200$  and  $\sim 4300$  Å, are the most affected by CN and CH features (see Figure 14 of Marino et al. 2008).

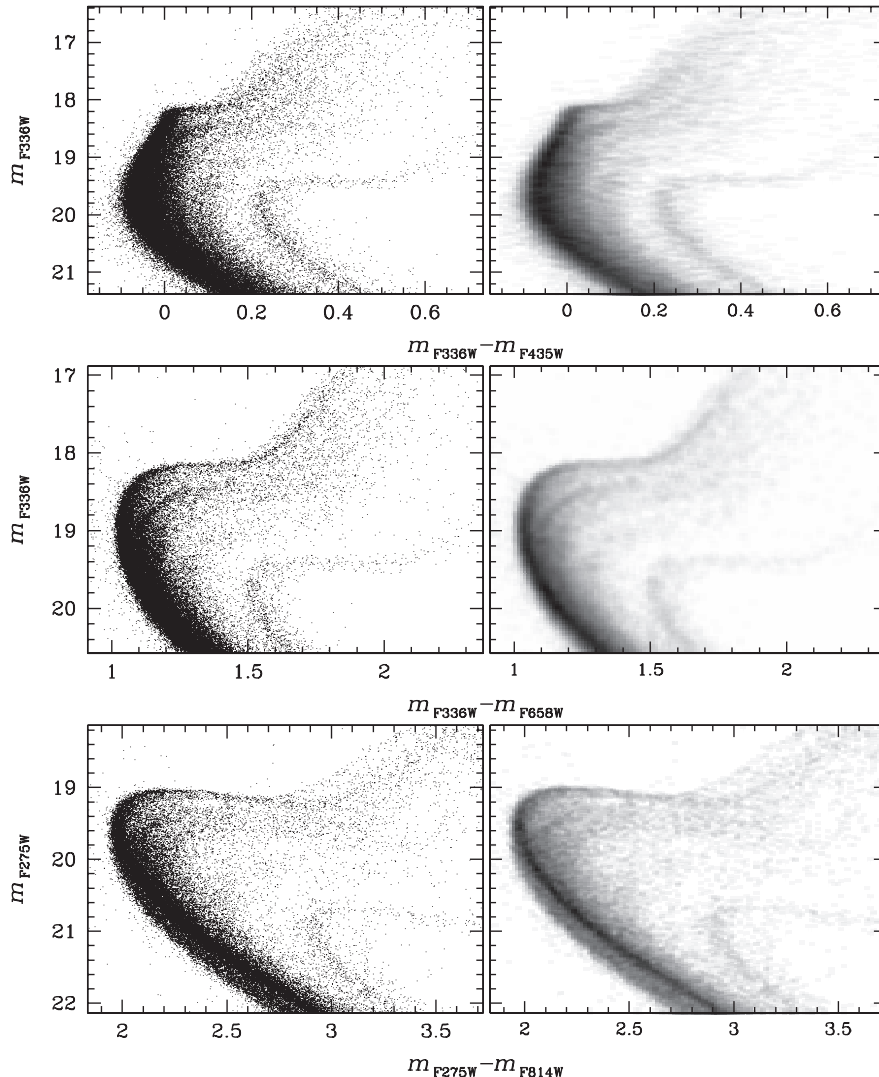


**Figure 11.** CMDs and corresponding Hess diagrams in different bands, focused around the SGB region.

Moreover, the He content must affect the position of the different MSs, as discussed in previous sections. Panel (a) of Figure 9 shows the  $m_{\text{F}336\text{W}}$  versus  $m_{\text{F}336\text{W}} - m_{\text{F}435\text{W}}$  CMD of  $\omega$  Cen. The MS-a fiducial sequence (drawn by eye) is plotted in red in panel (b). We subtracted the color of this fiducial sequence from the color of all the stars at the same magnitude. The rectified MSs are presented in panel (c) of Figure 9. We restricted our analysis to the magnitude interval  $19.7 < m_{\text{F}336\text{W}} < 21.4$ , where MS-a can easily be separated from the other MSs. We drew a vertical line, located at  $\Delta(m_{\text{F}336\text{W}} - m_{\text{F}435\text{W}}) = -0.065$ , to isolate MS-a members (on the right) from the rest of the MSs (on the left, hereafter called (b+r)MS for simplicity). We defined three radial intervals in such a way that each radial bin contains the same amount of selected stars (panel (d)). For each of the three radial intervals, using a logarithmic scale to emphasize MS-a counts, panel (e) plots the distribution of the rectified colors. The ratios of the star counts of MS-a/(b+r)MS are plotted in panel (f) as a function of the angular distance from the cluster center. Errors are calculated as in Bellini et al. (2009): for each radial interval, we derived the MS-a/(b+r)MS ratio in five magnitude bins (as defined by the red horizontal lines in panel (c)), and we used the corresponding number of stars as weight to compute a weighted mean for the MS-a/(b+r)MS

ratio in each of the five bins. Finally, we derived an error for the entire radial interval from the residuals of the individual ratio values from their mean, using the same weights as we had used for the mean. The radial trend shown in panel (f) of Figure 9 is consistent, within the errors, with the flat radial distribution of RGB-a stars (the progeny of the MSa stars) with respect to (RGB-MInt+RGB-MP) ones (as found by Bellini et al. 2009) within the inner  $\sim 2'$  from the cluster center.

#### 3.4. The Sub-giant and Lower Red Giant Branches

This region of the CMD was previously analyzed by Sollima et al. (2005) and by V07. The latter studied the  $m_{\text{F}435\text{W}}$  versus  $m_{\text{F}435\text{W}} - m_{\text{F}625\text{W}}$  ACS/WFC CMD. They identified four distinct stellar groups (named, from bright to faint magnitudes, A, B, C, and D; see Figure 2) corresponding to at least four distinct stellar populations, plus a broad distribution of stars, between groups C and D.

WFC3 photometry reveals a new, much more complex picture of the SGB region. In the  $m_{\text{F}275\text{W}}$  versus  $m_{\text{F}275\text{W}} - m_{\text{F}814\text{W}}$  CMD of Figures 10 and 11, stars of the original B and C components of V07 are widely spread in the F275W band, without any apparent substructure, while the brightest SGB component (A)

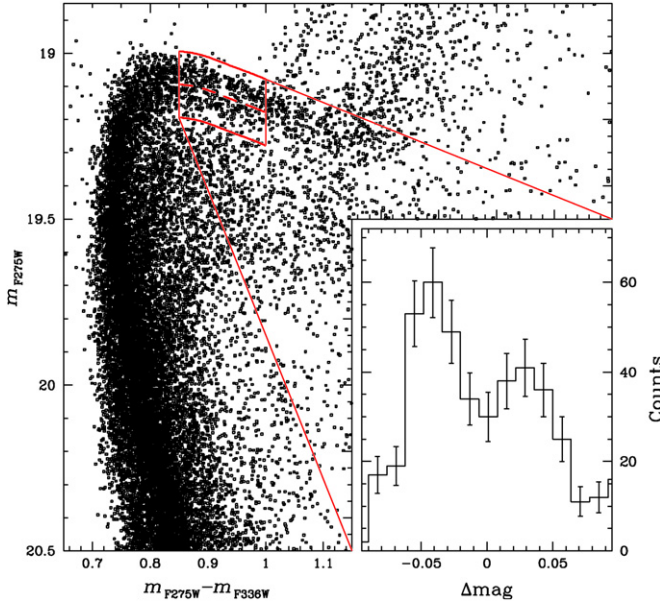


**Figure 12.** Zoom-in of the SGB in the  $m_{\text{F}275\text{W}}$  vs.  $m_{\text{F}275\text{W}} - m_{\text{F}336\text{W}}$  CMD. On the lower right is a histogram of the magnitude difference between the stars inside the red box and the magnitude of the dashed line, at the same color as the stars (see the text for more details).

(A color version of this figure is available in the online journal.)

is split into two branches. Figure 12 shows a more quantitative analysis of the split of SGB-A. The dashed red line has been traced (by hand) between the two branches of SGB-A. For each star in the red box that includes the dashed line, we calculated the difference between the star magnitude and the magnitude of the dashed line at the same color as the star. The bimodal distribution of these magnitude differences shown by the histogram in the lower part of Figure 12 confirms the presence of two distinct branches.

It is not clear how the two SGB-A sequences evolve into the RGB, though in the middle panels of Figure 11 they seem to run parallel up to the bright part of the RGB. In particular, the origin of the bluest RGB is not obvious: is it coming from SGB-B or from the faintest SGB of SGB-A? The bluest RGB could also be something similar to the broadened RGB of M4 visible in Figure 11 of Marino et al. (2008), where the broadening has been related to a spread in CNO affecting the  $U$  band. Only chemical abundance measurements will allow us to answer this question. Interestingly enough, the separation of the different RGB sequences becomes more visible in the CMD  $m_{\text{F}275\text{W}}$  versus  $m_{\text{F}275\text{W}} - m_{\text{F}814\text{W}}$  (see Figure 11).

There is another feature of the SGB which is visible for the first time in the CMDs presented in this paper. The SGB-D of V07 (which corresponds to the SGB-a of Ferraro et al. 2004) is also broadened, as shown in Figures 10 and 11 and, in more detail, in Figure 13. It is not clear whether this broadening

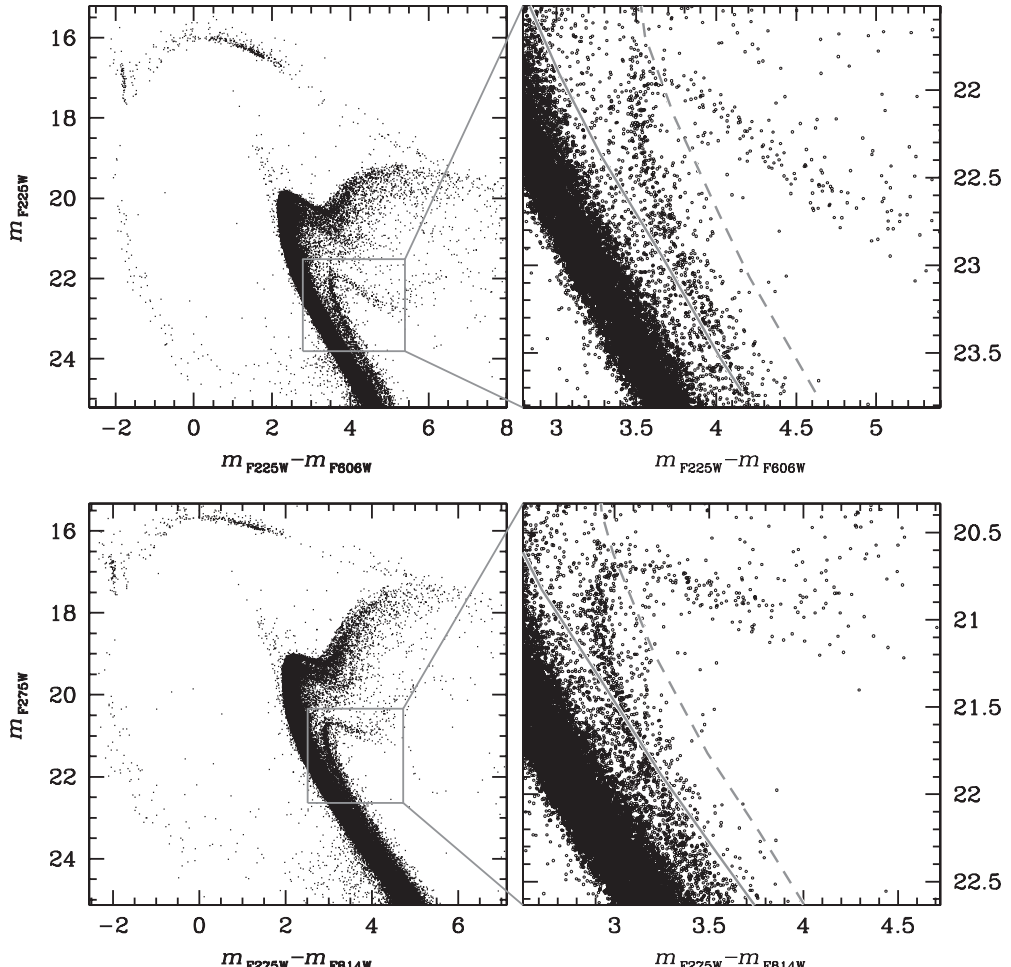


**Figure 13.** Zoom-in of two CMDs around the SGB-D region showing hints of two sub-groups.

**Table 3**  
First Lines of the Electronically Available Catalog

ID	R.A. (J2000.0)	Decl. (J2000.0)	X	Y	$m_{\text{F}225\text{W}}$	$m_{\text{F}275\text{W}}$	$m_{\text{F}336}$	$m_{\text{F}435\text{W}}$	$m_{\text{F}606\text{W}}$	$m_{\text{F}625\text{W}}$	$m_{\text{F}658\text{N}}$	$m_{\text{F}814\text{W}}$
1	201.7162676	-47.5126489	1781.197	426.673	23.421	22.291	21.088	20.971	19.990	19.760	19.526	19.311
2	201.7156870	-47.5123958	1809.429	444.904	20.674	19.843	19.095	19.166	18.436	18.248	18.056	17.886
3	201.7142821	-47.5123325	1877.748	449.480	21.045	20.157	19.368	19.426	18.650	18.468	18.271	18.092
4	201.7150112	-47.5122876	1842.291	452.709	24.545	22.899	21.604	21.380	20.289	20.133	19.908	19.579
5	201.7138235	-47.5122802	1900.054	453.253	23.926	22.485	21.130	21.040	20.033	19.801	19.578	19.333
6	201.7158384	-47.5122430	1802.055	455.906	21.261	20.377	19.555	19.596	18.831	18.625	18.421	18.248
7	201.7153042	-47.5121646	1828.040	461.554	21.184	20.318	19.513	19.597	18.803	18.633	18.426	18.202
8	201.7150457	-47.5121237	1840.615	464.507	21.843	20.906	20.033	20.095	19.282	19.092	18.866	18.681
9	201.7166455	-47.5121043	1762.811	465.879	21.047	20.206	19.413	19.500	18.726	18.548	18.340	18.132
10	201.7164538	-47.5120773	1772.129	467.827	21.519	20.593	19.773	19.820	19.058	18.870	18.676	18.444
...	...	...	...	...	...	...	...	...	...	...	...	...

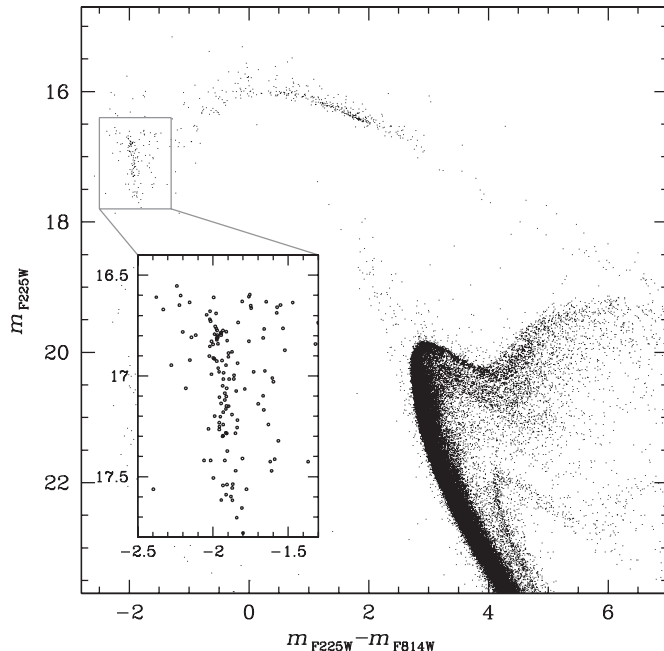


**Figure 14.**  $m_{\text{F}225\text{W}}$  vs.  $m_{\text{F}225\text{W}} - m_{\text{F}814\text{W}}$  CMD best highlights the complex morphology of the HB. The inset shows a zoom-in of the blue hook section of the HB. Two distinct and almost parallel features are visible.

corresponds to two distinct populations. A visual inspection of all these figures suggests that the faintest part of SGB-D could be associated with a poorly populated MS which runs on the red side of the MS-a. The sequence on the red side of the MS-a cannot be a sequence of binaries, which would evolve into a brighter (not fainter) SGB.

In summary, the new WFC3 photometry shows that the SGB of  $\omega$  Cen is even more complex than previously thought. There are at least six distinct sequences, plus the broad distribution of stars between SGB-C and SGB-D already identified by V07.

### 3.5. The Horizontal Branch

Typically, the horizontal branch (HB) amplifies all the complexities of a stellar population, and it is no different for  $\omega$  Cen. Indeed, the HB shown in Figure 14 shows a multiplicity of features and, in particular, a well-known, very extended HB, with a pronounced blue hook (D'Cruz et al. 2000). In this section, we want to focus our attention on the blue hook.

The blue hook has a complex morphology, and it has been already studied by Cassisi et al. (2009) and D'Antona et al. (2010), using the current ACS/WFC data set from O-9442. The

interesting new feature displayed by the WFC3/UVIS data set, and clearly shown in the inset of Figure 14, is that the blue hook is split into two distinct, well-defined, separated—and almost vertical—sequences. The bluer blue-hook sequence contains  $80\% \pm 5\%$  of the total blue hook population, while the remaining  $20\% \pm 5\%$  of blue hook stars populate a redder parallel sequence shifted by about 0.3 mag in the  $m_{\text{F}275\text{W}} - m_{\text{F}814\text{W}}$  color.

We also note that, on the red side of the two blue hooks (see Figure 14), the HB seems to be separated into a fainter (more populated) and a brighter component, up to at least  $m_{\text{F}275\text{W}} - m_{\text{F}814\text{W}} = 0.4$ .

## 4. ELECTRONIC CATALOG

The astrophotometric catalog is available online from the SIMBAD database.<sup>7</sup> Table 3 shows the first entries of the catalog. Column (1) contains star IDs, Columns (2) and (3) give the J2000.0 equatorial coordinates in decimal degrees, and Columns (4) and (5) provide the pixel coordinates  $x$  and  $y$  of the distortion-corrected reference meta-chip. Columns (6) through (13) contain photometric measurements. Note that the public catalog gives the original photometry. The reddening and photometric zero-point spatial variation corrected photometry is available from the authors upon request.<sup>8</sup>

We thank S. Cassisi, F. D'Antona, and R. Gratton for useful discussions. A.B. acknowledges support by the CA.RI.PA.RO. foundation, and by the STScI under the “2008 Graduate Research Assistantship” program. G.P., A.F.M., and A.P.M. acknowledge partial support by MIUR under the program PRIN2007 (prot. 20075TP5K9) and by ASI under the program ASI-INAF I/016/07/0.

## REFERENCES

- Anderson, J. 1997, PhD thesis, Univ. California, Berkeley
- Anderson, J., Bedin, L. R., Piotto, G., Yadav, R. S., & Bellini, A. 2006, *A&A*, **454**, 1029
- Anderson, J., Piotto, G., King, I. R., Bedin, L. R., & Guhathakurta, P. 2009, *ApJ*, **697**, L58
- Anderson, J., et al. 2008, *AJ*, **135**, 2055
- Bedin, L. R., Piotto, G., Anderson, J., Cassisi, S., King, I. R., Momany, Y., & Carraro, G. 2004, *ApJ*, **605**, L125
- Bedin, L. R., Cassisi, S., Castelli, F., Piotto, G., Anderson, J., Salaris, M., Momany, Y., & Pietrinferni, A. 2005, *MNRAS*, **357**, 1038
- Bekki, K., & Freeman, K. C. 2003, *MNRAS*, **346**, L11

<sup>7</sup> <http://simbad.u-strasbg.fr/simbad>

<sup>8</sup> Note that this work is based on images taken in 2009 July. New WFC3/UVIS epochs have been (and others will soon be) collected for the same field of  $\omega$  Cen analyzed here.

- Bellini, A., & Bedin, L. R. 2009, *PASP*, **121**, 1419  
 Bellini, A., Piotto, G., Bedin, L. R., King, I. R., Anderson, J., Milone, A. P., & Momany, Y. 2009, *A&A*, **507**, 1393  
 Cannon, R. D., & Stobie, R. S. 1973, *MNRAS*, **162**, 207  
 Cassisi, S., Salaris, M., Anderson, J., Piotto, G., Pietrinferni, A., Milone, A., Bellini, A., & Bedin, L. R. 2009, *ApJ*, **702**, 1530  
 D'Antona, F., Caloi, V., & Ventura, P. 2010, *MNRAS*, **405**, 2295  
 D'Cruz, N. L., et al. 2000, *ApJ*, **530**, 352  
 Ferraro, F. R., Sollima, A., Pancino, E., Bellazzini, M., Straniero, O., Origlia, L., & Cool, A. M. 2004, *ApJ*, **603**, L81  
 Freeman, K. C., & Rodgers, A. W. 1975, *ApJ*, **201**, L71  
 Harris, W. E. 1996, *AJ*, **112**, 1487  
 Johnson, C. I., Pilachowski, C. A., Rich, R. M., & Fulbright, C. P. 2009, *ApJ*, **698**, 2048  
 Lee, J.-W., Kang, Y.-W., Lee, J., & Lee, Y.-W. 2009, *Nature*, **462**, 480  
 Lee, Y.-W., Joo, J.-M., Sohn, Y.-J., Rey, S.-C., Lee, H.-C., & Walker, A. R. 1999, *Nature*, **402**, 55  
 Lee, Y.-W., et al. 2005, *ApJ*, **621**, L57  
 Marino, A. F., Villanova, S., Piotto, G., Milone, A. P., Momany, Y., Bedin, L. R., & Medling, A. M. 2008, *A&A*, **490**, 625  
 Milone, A. P., Bedin, L. R., Piotto, G., & Anderson, J. 2009, *A&A*, **497**, 755  
 Milone, A. P., et al. 2008, *ApJ*, **673**, 241  
 Milone, A. P., et al. 2010, *ApJ*, **709**, 1183  
 Norris, J. E. 2004, *ApJ*, **612**, L25  
 Pancino, E., Ferraro, F. R., Bellazzini, M., Piotto, G., & Zoccali, M. 2000, *ApJ*, **534**, L83  
 Pancino, E., Pasquini, L., Hill, V., Ferraro, F. R., & Bellazzini, M. 2002, *ApJ*, **568**, L101  
 Piotto, G., et al. 2005, *ApJ*, **621**, 777  
 Sarajedini, A., et al. 2007, *AJ*, **133**, 1658  
 Sollima, A., Ferraro, F. R., Bellazzini, M., Origlia, L., Straniero, O., & Pancino, E. 2007, *ApJ*, **654**, 915  
 Sollima, A., Pancino, E., Ferraro, F. R., Bellazzini, M., Straniero, O., & Pasquini, L. 2005, *ApJ*, **634**, 332  
 Villanova, S., et al. 2007, *ApJ*, **663**, 296